



Article submitted to journal

Subject Areas:

Sun: filaments, prominences

Keywords:instabilities, magnetic fields,
simulations**Author for correspondence:**

B. Popescu Braileanu

e-mail:

[beatriceannemone.popescubraileanu](mailto:beatriceannemone.popescubraileanu@kuleuven.be)[@kuleuven.be](mailto:beatriceannemone.popescubraileanu@kuleuven.be)Radiative loss and ion-neutral
collisional effects in
astrophysical plasmasB. Popescu Braileanu¹, R. Keppens¹¹ Centre for mathematical Plasma Astrophysics,
Department of Mathematics, KU Leuven,
Celestijnenlaan 200B, 3001 Leuven, Belgium

In this paper we study the role of radiative cooling in a two-fluid model consisting of coupled neutrals and charged particles. We first analyze the linearized two-fluid equations where we include radiative losses in the energy equation for the charged particles. In a 1D geometry for parallel propagation and in the limiting cases of weak and strong coupling, it can be shown analytically that the instability conditions for the thermal mode and the sound waves, the isobaric and isentropic criteria, respectively, remain unchanged with respect to one-fluid radiative plasmas. For the parameters considered in this paper, representative for the solar corona, the radiative cooling produces growth of the thermal mode and damping of the sound waves. In the weak coupling limit, the growth of the thermal instability and the damping of the sound waves is as derived in [Field \(1965\)](#) using the charged fluid properties. When neutrals are included and are sufficiently coupled to the charges, the thermal mode growth rate and the wave damping both reduce by the same factor, which depends on the ionization fraction only. For a heating function which is constant in time, we find that the growth of the thermal mode and the damping of the sound waves are slightly larger. The numerical calculation of the eigenvalues of the general system of equations in a 3D geometry confirm the analytic results. We then run 2D fully nonlinear simulations which give consistent results: a higher ionization fraction or lower coupling will increase the growth rate. The magnetic field contribution is negligible in the linear phase. Ionization-recombination effects might play an important role because the radiative cooling produces a large range of temperatures in the system. In the numerical simulation, after the first condensation phase, when the minimum temperature is reached, the fraction of neutrals increases four orders of magnitude because of the recombination.

© The Authors. Published by the Royal Society under the terms of the Creative Commons Attribution License <http://creativecommons.org/licenses/by/4.0/>, which permits unrestricted use, provided the original author and source are credited.

1. Introduction

Partial ionization effects are important in many astrophysical contexts. In the solar atmosphere ion-neutral collisions become important in the regions where a cool dense mostly neutral plasma changes to a tenuous hot and ionized plasma. This is the case of the solar chromosphere, but also in prominence-corona transition regions. It is usually assumed that in prominences the ionization is collisional and the recombination is produced by radiative processes (Parenti, S. et al., 2019). At the same time, many recent works (e.g. Antiochos, Klimchuk, 1991; Antolin, 2020; Brughmans et al., 2022; Claes, Keppens, 2019; Hermans, J., Keppens, R., 2021; Jenkins, Keppens, 2021; Jerčić, Keppens, 2023; Klimchuk et al., 2010; Li et al., 2022, 2023; Liakh, Keppens, 2023; Luna et al., 2012; Schrijver, 2001; Xia et al., 2017; Zhou et al., 2023) support the original claim by Parker (1953) that thermal instability is a fundamental process that can trigger in-situ condensations, like prominences and coronal rain in the solar atmosphere, but also denser clumps in galactic winds, or in other astrophysical contexts (Gronke, Oh, 2023; Proga et al., 2022; Waters et al., 2022). For this reason, the linear mode which grows exponentially due to the energy loss is usually called “thermal” or “condensation” mode (see Field, 1965). Here, we will revisit the fundamental theory behind thermal instability initiated by Parker (1953) and Field (1965), but this time extend the findings to neutral-plasma mixtures, which play a role for especially the finer-scale details of the prominence or coronal rain dynamics (Popescu Braileanu et al., 2023, 2021a,b; Terradas et al., 2021).

It was shown that the magnetic field does not affect significantly the behaviour of the thermal mode (Field, 1965). From the linear analysis the motion in the condensation mode is mostly along the field lines, therefore they do not produce perturbations of the magnetic field. It was shown analytically that, when the propagation is not exactly perpendicular, the magnetic field has no effect on the linear growth of the thermal mode and the magnetic field with magnitude at equipartition value is enough to align the small motions of the condensation mode with the field (Field, 1965). However, for exactly perpendicular propagation, it is shown analytically that the perturbation in the magnetic pressure is not zero and has a slight stabilizing effect on the linear growth of the thermal mode (Field, 1965). The non-linear evolutions show systematic field-guided motions of the condensations (Claes, Keppens, 2019). The shape and evolution of the condensations depend on the radiative cooling curve used (Hermans, J., Keppens, R., 2021).

The effect of partial ionization on wave propagation in a uniform atmosphere has been studied by several authors (Soler et al., 2013b; Soler et al., 2013a). The authors find cutoff values for the Alfvén and magnetoacoustic waves because of the frictional force competing with the restoring force. In these works the dispersion relation obtained analytically was studied numerically and some simplifications were done, such as including the ion-neutral coupling only in the momentum equation. We here augment these findings with an emphasis on thermal instabilities, and by allowing both thermal (energy) and momentum coupling. The partial ionization effects were studied in the dynamics of falling blobs, with properties characteristic for coronal rain (Martínez-Gómez et al., 2022; Oliver et al., 2016), however, the radiative cooling effect was not included and the formation of these blobs was not considered in their study.

In ion-neutral mixtures, one should consider ionization-recombination aspects as well. They may enter especially during non-linear evolutions, as it was found that ionization-recombination processes do not modify the linear growth of the Rayleigh-Taylor instability, but during the non-linear phase the neutral drops become surrounded by a layer of ionized material (Popescu Braileanu et al., 2021b). It was also shown that ionization and recombination processes alter significantly the structure of a two-fluid slow shock (Snow, B., Hillier, A., 2021). Here, we will consider ionization-recombination effects in non-linear evolutions of thermally unstable setups. The very large temperatures in the solar corona makes the gravitational scale height very large, of several hundreds of megameters for a temperature of one million K. Therefore, for the study of scales similar to one megameter, neglecting gravity and considering the density and pressure uniform is a good approximation. This simplifies the setups we use for our nonlinear studies.

In this work we include the thermal exchange between charges and neutrals in both energy equations, as well as radiative cooling in the charged energy equation. We solve the dispersion relation numerically and we study the effect of the collisions and the radiative losses on damping the waves and the growth of the thermal mode. We then test the linear analytical results with simulations where we can also study the non-linear evolution. In order to see the development of the two-fluid thermal instability in the nonlinear phase, we perform fully nonlinear 2D, two-fluid simulations, using the same uniform background.

2. Governing equations

The radiative cooling term is in general a function of temperature and density, $F(\rho, T)$. If we consider a background atmosphere with density ρ_0 and temperature T_0 in thermal equilibrium, the radiative losses have to be compensated by an unspecified heating function so that:

$$F(\rho_0, T_0) = 0. \quad (2.1)$$

Usually, this term is written as (see [Field, 1965](#)),

$$F(\rho, T) = \rho \mathcal{L}(\rho, T), \quad (2.2)$$

where $\mathcal{L}(\rho, T)$ is a generalized heat-loss function which fulfills:

$$\mathcal{L}(\rho_0, T_0) = 0 \quad (2.3)$$

for the thermal equilibrium condition, and it is usually considered to be for the optically thin radiative loss prescription:

$$\mathcal{L}(\rho_0, T_0) = \rho \Lambda(T) - \rho_0 \Lambda_0, \quad (2.4)$$

where the cooling curve, Λ , is a function of temperature only. The subindex $_0$ means that the quantity has to be evaluated for the background atmosphere variables. Therefore the contribution of the radiative cooling terms in the energy equation becomes:

$$F(\rho, T) = \rho [\rho \Lambda - \rho_0 \Lambda_0], \quad (2.5)$$

thus having a time-varying heating function which depends on the time-varying density, rather than on equilibrium variables only. In our simulations, however, we considered a constant heating function (see [Claes, Keppens, 2019](#); [Hermans, J., Keppens, R., 2021](#)), having the contribution of the radiative losses, when the background is in thermal equilibrium actually given by

$$F(\rho, T) = \rho^2 \Lambda - \rho_0^2 \Lambda_0. \quad (2.6)$$

The nonlinear two-fluid equations evolved by the code `MP1-AMRVAC` ([Keppens et al., 2023](#)), when we split the variables (see [Yadav, N. et al., 2022](#)) into time-dependent (subscript “1”) and time-independent variables (subscript “0”) for neutral and charged densities, neutral and charged pressures, and the magnetic field, become with the splitting obeying

$$\begin{aligned} \rho_n &= \rho_{n0} + \rho_{n1}, \rho_c = \rho_{c0} + \rho_{c1}, p_n = p_{n0} + p_{n1}, p_c = p_{c0} + p_{c1}, \mathbf{B} = \mathbf{B}_0 + \mathbf{B}_1, \\ \frac{\partial \rho_{n0}}{\partial t} &= 0, \frac{\partial \rho_{c0}}{\partial t} = 0, \frac{\partial p_{n0}}{\partial t} = 0, \frac{\partial p_{c0}}{\partial t} = 0, \frac{\partial \mathbf{B}_0}{\partial t} = 0, \end{aligned} \quad (2.7)$$

as follows:

$$\frac{\partial \rho_{n1}}{\partial t} + \nabla \cdot (\rho_n \mathbf{v}_n) = S_n, \quad (2.8)$$

$$\frac{\partial \rho_{c1}}{\partial t} + \nabla \cdot (\rho_c \mathbf{v}_c) = -S_n, \quad (2.9)$$

$$\frac{\partial(\rho_n \mathbf{v}_n)}{\partial t} + \nabla \cdot (\rho_n \mathbf{v}_n \mathbf{v}_n + p_{n1} \mathbb{I}) = \rho_{n1} \mathbf{g} + \mathbf{R}_n, \quad (2.10)$$

$$\begin{aligned} \frac{\partial(\rho_c \mathbf{v}_c)}{\partial t} + \nabla \cdot \left[\rho_c \mathbf{v}_c \mathbf{v}_c + \left(p_{c1} + \frac{B_1^2}{2} + \mathbf{B}_0 \cdot \mathbf{B}_1 \right) \mathbb{I} - \mathbf{B}_1 \mathbf{B}_1 - \mathbf{B}_1 \mathbf{B}_0 - \mathbf{B}_0 \mathbf{B}_1 \right] \\ = \rho_{c1} \mathbf{g} - \mathbf{R}_n, \end{aligned} \quad (2.11)$$

$$\frac{\partial}{\partial t} \left(e_{n1} + \frac{1}{2} \rho_n \mathbf{v}_n^2 \right) + \nabla \cdot \left[\mathbf{v}_n \left(e_n + \frac{1}{2} \rho_n \mathbf{v}_n^2 + p_{n1} \right) \right] = \rho_{n1} \mathbf{v}_n \cdot \mathbf{g} - p_{n0} \nabla \cdot \mathbf{v}_n + M_n, \quad (2.12)$$

$$\begin{aligned} \frac{\partial}{\partial t} \left(e_{c1} + \frac{1}{2} \rho_c \mathbf{v}_c^2 + \frac{B_1^2}{2} \right) + \nabla \cdot \left[\mathbf{v}_c \left(e_c + \frac{1}{2} \rho_c \mathbf{v}_c^2 + p_{c1} \right) - (\mathbf{v}_c \times \mathbf{B}) \times \mathbf{B}_1 \right] \\ = \rho_{c1} \mathbf{v}_c \cdot \mathbf{g} - p_{c0} \nabla \cdot \mathbf{v}_c + \mathbf{J}_0 \cdot (\mathbf{v}_c \times \mathbf{B}_1) - \rho_c^2 \Lambda + \rho_{c0}^2 \Lambda_0 - M_n, \end{aligned} \quad (2.13)$$

$$\frac{\partial \mathbf{B}_1}{\partial t} = \nabla \times (\mathbf{v}_c \times \mathbf{B}). \quad (2.14)$$

The above equations are written in non-dimensional units. \mathbb{I} is the identity matrix. The equations contain velocity fields for neutrals and charges, \mathbf{v}_n and \mathbf{v}_c . Terms S_n , \mathbf{R}_n and M_n in the above equations are the collisional coupling terms, implemented as described by Eqs. (6.1)-(6.3), shown in Appendix 6, being the same Eqs. (13) in Popescu Braileanu, B., Keppens, R. (2022), which introduce a basic coupling parameter called α , which quantifies collisional coupling. We considered the radiative losses in the charged energy equation Eq. (2.13). In the two-fluid model we use the same radiative losses curves which define the profile of Λ as a function of temperature, implemented for the MHD model (Hermans, J., Keppens, R., 2021), now calculated using the charged fluid temperature, $\Lambda = \Lambda(T_c)$. In the above equations it is assumed that the time-independent background is in mechanical equilibrium, fulfilling the magneto-hydrostatic equilibrium for the charged fluid and the hydrostatic equilibrium for the neutral fluid, meaning uniform charges and neutral pressures and force-free field (i.e. $\mathbf{J}_0 \times \mathbf{B}_0$) when there is no gravity (gravity is incorporated in the equations as implemented above where gravitational acceleration is \mathbf{g} , but we ignore it further on). Our background magnetic field will even be a simple uniform field \mathbf{B}_0 in what follows. We also assume that the background is in thermal equilibrium. We have the same background temperature for neutrals and charges, $T_{n0} = T_{c0} = T_0$, and the radiative losses of the equilibrium charged fluid is compensated by a heating mechanism, constant in time, which is explicitly removed from Eqs. (2.8)-(2.14) solved by code. Note that we did not incorporate anisotropic thermal conduction, and we adopt a simple ideal-gas-law closure for pressures p , internal energies e and temperatures T .

3. Linear approach

The time evolution of a set of small perturbations \mathbf{u} of a stationary background is assumed to be $\propto \exp(i\omega t)$ and the equations are linearized, becoming

$$\left(\hat{\mathbf{M}} - \omega \mathbb{I} \right) \mathbf{u} = 0, \quad (3.1)$$

where the elements of the complex matrix $\hat{\mathbf{M}}$ depend on the background values. The background has densities ρ_{c0} , ρ_{n0} , and pressures p_{c0} and p_{n0} , of charges and neutrals, respectively and a uniform magnetic field with magnitude B_0 . We introduce some quantities, the total density and pressure, the sound speed for neutrals, charges and total fluid, as well as the Alfvén, fast and slow

speeds of the charged fluid and the total fluid, calculated for the background values:

$$\rho_0 = \rho_{c0} + \rho_{n0}, \quad p_0 = p_{c0} + p_{n0} \quad (3.2)$$

$$c_{n0} = \sqrt{\gamma \frac{p_{n0}}{\rho_{n0}}}, \quad (3.3)$$

$$c_{c0} = \sqrt{\gamma \frac{p_{c0}}{\rho_{c0}}}, \quad (3.4)$$

$$c_{t0} = \sqrt{\gamma \frac{p_0}{\rho_0}}, \quad (3.5)$$

$$v_{Ac0} = \frac{B_0}{\sqrt{\rho_{c0}}}, \quad (3.6)$$

$$v_{At0} = \frac{B_0}{\sqrt{\rho_0}}, \quad (3.7)$$

$$f_{c0} = \sqrt{\frac{1}{2} \left[v_{Ac0}^2 + c_{c0}^2 + \sqrt{(v_{Ac0}^2 + c_{c0}^2)^2 - 4v_{Ac0}^2 c_{c0}^2 \cos^2(\theta)} \right]}, \quad (3.8)$$

$$f_{t0} = \sqrt{\frac{1}{2} \left[v_{At0}^2 + c_{t0}^2 + \sqrt{(v_{At0}^2 + c_{t0}^2)^2 - 4v_{At0}^2 c_{t0}^2 \cos^2(\theta)} \right]}, \quad (3.9)$$

$$s_{c0} = \sqrt{\frac{1}{2} \left[v_{Ac0}^2 + c_{c0}^2 - \sqrt{(v_{Ac0}^2 + c_{c0}^2)^2 - 4v_{Ac0}^2 c_{c0}^2 \cos^2(\theta)} \right]}, \quad (3.10)$$

$$s_{t0} = \sqrt{\frac{1}{2} \left[v_{At0}^2 + c_{t0}^2 - \sqrt{(v_{At0}^2 + c_{t0}^2)^2 - 4v_{At0}^2 c_{t0}^2 \cos^2(\theta)} \right]}. \quad (3.11)$$

In a 3D cartesian geometry, without loss of generality, we choose the magnetic field \mathbf{B}_0 in the xz plane and the direction of propagation in the x -direction. For a uniform background, the perturbations from Eq. (3.1) can be written as:

$$\mathbf{u} = (\rho_{c1}, \rho_{n1}, v_{cx}, v_{nx}, v_{cy}, v_{ny}, v_{cz}, v_{nz}, p_{c1}, p_{n1}, B_{x1}, B_{y1}, B_{z1})^T \exp [i(\omega t - k_x x)], \quad (3.12)$$

k_x is the wavenumber or spatial frequency and ω represents the temporal frequency. In our study, k_x is a real quantity and ω is complex. The linearized two-fluid equations for a static background

become:

$$\begin{aligned}
\omega\rho_{c1} - k_x\rho_{c0}v_{cx} &= 0, \\
\omega\rho_{n1} - k_x\rho_{n0}v_{nx} &= 0, \\
i\omega\rho_{c0}v_{cx} - ik_x p_{c1} - ik_x B_{z0}B_{z1} + \alpha\rho_{c0}\rho_{n0}(v_{cx} - v_{nx}) &= 0, \\
i\omega\rho_{n0}v_{nx} - ik_x p_{n1} - \alpha\rho_{c0}\rho_{n0}(v_{cx} - v_{nx}) &= 0, \\
i\omega\rho_{c0}v_{cy} + ik_x B_{y1}B_{x0} + \alpha\rho_{c0}\rho_{n0}(v_{ny} - v_{cy}) &= 0, \\
i\omega\rho_{n0}v_{ny} - \alpha\rho_{c0}\rho_{n0}(v_{ny} - v_{cy}) &= 0, \\
i\omega\rho_{c0}v_{cz} + ik_x B_{z1}B_{x0} + \rho_{c0}\alpha\rho_{n0}(v_{cz} - v_{nz}) &= 0, \\
i\omega\rho_{n0}v_{nz} - \alpha\rho_{c0}\rho_{n0}(v_{cz} - v_{nz}) &= 0, \\
i\omega p_{c1} - ic_{c0}^2\omega\rho_{c1} + (\gamma - 1) \left[\frac{1}{2}(\rho_{c0}p_{c1} - p_{c0}\rho_{c1}) \frac{d\Lambda_0}{dT} + 2\rho_{c0}\rho_{c1}\Lambda_0 \right] \\
+ \alpha \left[-\rho_{c1}p_{n0} - \rho_{c0}p_{n1} + \frac{1}{2}(\rho_{n1}p_{c0} + \rho_{n0}p_{c1}) \right] &= 0, \\
i\omega p_{n1} - ic_{n0}^2\omega\rho_{n1} - \alpha \left[-\rho_{c1}p_{n0} - \rho_{c0}p_{n1} + \frac{1}{2}(\rho_{n1}p_{c0} + \rho_{n0}p_{c1}) \right] &= 0, \\
B_{x1} &= 0, \\
B_{y1}\omega + B_{x0}k_x v_{cy} &= 0, \\
B_{z1}\omega - B_{z0}k_x v_{cx} + B_{x0}k_x v_{cz} &= 0. \tag{3.13}
\end{aligned}$$

where the unknowns are the complex amplitudes of the perturbations, as shown in Eq. (3.12). γ is the ratio of specific heats.

We believe that, similarly to the case of the Rayleigh-Taylor instability (Popescu Braileanu et al., 2021b), the ionization/recombination processes are not important in the linear phase, and ignored them here to keep the model simpler. While we neglected ionization/recombinations in the two-fluid model in the linear analysis, we included the elastic collisions in the momentum equations and the thermal exchange in the energy equations, i.e. all terms containing the coupling parameter α .

The linearized form of $F(\rho, T)$ from Eq. (2.6) around background density and temperature values ρ_0 and T_0 is:

$$F(\rho, T) = \frac{\partial F_0}{\partial \rho} \rho_1 + \frac{\partial F_0}{\partial T} T_1. \tag{3.14}$$

In the linear assumption, for a generic equation of state written in non-dimensional form as $p = A\rho T$, where A is the inverse of the non-dimensional mean molecular weight (see also Eq. (14) in Field, 1965),

$$T_1 = \frac{1}{A\rho_0} \left(p_1 - p_0 \frac{\rho_1}{\rho_0} \right). \tag{3.15}$$

This gives the contribution of the radiative cooling term in the linearized equation for F defined in Eq. (2.6):

$$F(\rho, T) = 2\rho_0\Lambda_0\rho_1 + \frac{1}{A} \frac{\partial \Lambda_0}{\partial T} (p_1\rho_0 - p_0\rho_1). \tag{3.16}$$

The difference from considering a constant heating function instead of a time-varying heating function, having F as defined in Eq. (2.6) rather than the definition in Eq. (2.5), is the factor of 2 multiplying the term containing Λ_0 , compared to Eq. (13) in Field (1965) and Eq. (9) in Claes, Keppens (2019). We will see how the analytic expressions are slightly modified by this choice, as we will highlight this factor 2 in the following derivation. We used the results for the constant heating function in our analysis in order to have full consistency with the equations solved by the code.

In the two-fluid model, the radiative cooling (RC) term is added in the charges energy equation Eq. (2.13), similarly to MHD, but using charged fluid density and temperature in the evaluation of the term. The RC is considered for high temperature plasmas optically thin, where the plasma is fully ionized, so that the radiative losses are related to the charged particles. We assume Hydrogen only and charge neutrality, therefore $A = 2$ for the charged fluid in the above Eq. (3.16).

The collisional parameter α depends weakly on plasma parameters, being proportional to the square root of the average temperature between neutrals and charges. It is assumed constant, calculated using equilibrium values, in the above linearized Eqs. (3.13).

The system Eqs. (3.13) has 13 equations, but the x -induction equation does not contain ω because of the additional constraint of zero magnetic field divergence (in the linear assumption one of the induction equations is equivalent to the zero divergence of the magnetic field), therefore there are 12 solutions for the eigenvalue problem Eq. (3.1). When there is no coupling between the charges and neutrals, there are five neutral modes and seven MHD modes divided in two trivial entropy modes, six propagating modes for the charged fluid: fast, slow and Alfvén; two propagating sound modes and two trivial shear modes for the neutral fluid (Goedbloed et al., 2019).

We can also observe in the Eqs. (3.13) that the y -momentum equations for neutrals and charges and the y -induction equation are decoupled from the rest. Therefore the Alfvén branch decouples:

$$B_{x0}^2 k_x^2 (\omega - i\alpha\rho_{c0}) - \omega^2 \rho_{c0} [\omega - i\alpha(\rho_{c0} + \rho_{n0})] = 0, \quad (3.17)$$

and the non-ideal terms in the energy equations (the thermal exchange and radiative cooling) do not affect the Alfvén waves. Eq. (3.17) is equivalent to Eq. (14) from Soler et al. (2013a) and Eq. (39) in Popescu Braileanu et al. (2019). The remaining equation, of 9th order is not shown here because of its complicated form, however with some additional assumptions it particularizes into some known forms. When the radiative cooling is not taken into account, the charges entropy mode decouples, giving the root $\omega = 0$.

The angle between the wavevector \mathbf{k} and \mathbf{B}_0 can equivalently be described using the following transformations:

$$k_x = k, B_{z0} = \frac{k_{\perp}}{k} B_0, B_{x0} = \frac{k_{\parallel}}{k} B_0, k_{\perp} = k \sin(\theta), k_{\parallel} = k \cos(\theta), \quad (3.18)$$

where we introduce field-aligned parallel and field-perpendicular wave numbers. We will now discuss various limits of the dispersion relation.

(a) The case of purely perpendicular propagation and no radiative cooling

In this case, regardless the value of k , we obtain a triple trivial root $\omega = 0$, a purely damped root $\omega = i\alpha(\rho_{c0} + \rho_{n0})$ and the remaining fifth order dispersion relation becomes

$$\begin{aligned} v_{Ac0}^2 k^2 \left[-2\omega^3 - i\alpha k^2 p_{c0} + \alpha^2 \omega \rho_{c0} (2\rho_{c0} + \rho_{n0}) + i\alpha \omega^2 (4\rho_{c0} + \rho_{n0}) + c_{n0}^2 k^2 (2\omega - i\alpha \rho_{n0}) \right] + \\ c_{c0}^2 k^2 \left[2c_{n0}^2 k^2 \omega - 2\omega^3 - i\alpha k^2 p_{c0} + 4i\alpha \omega^2 \rho_{c0} + \alpha^2 \omega \rho_{c0} (2\rho_{c0} + \rho_{n0}) \right] + \\ c_{n0}^2 k^2 \left[-2\omega^3 - 2i\alpha k^2 p_{n0} + 3i\alpha \omega^2 \rho_{n0} + \alpha^2 \omega \rho_{n0} (2\rho_{c0} + \rho_{n0}) \right] + \\ \omega^2 (2\omega^3 + i\alpha k^2 (p_{c0} + 2p_{n0}) - i\alpha \omega^2 (4\rho_{c0} + 3\rho_{n0}) - \alpha^2 \omega (2\rho_{c0}^2 + 3\rho_{c0}\rho_{n0} + \rho_{n0}^2)) = 0 \end{aligned} \quad (3.19)$$

We used the equilibrium charged fluid Alfvén speed, the neutral and charged fluid sound speeds, introduced in Eqs. (3.6), (3.3), (3.4), respectively, and $k \equiv k_{\perp}$. When the coupling is taken into account only in the momentum equations, but not in the energy equation (i.e. when the thermal exchange is neglected), another root $\omega = 0$ is obtained and the then remaining fourth order dispersion relation reduces to

$$(c_{c0}^2 + v_{Ac0}^2) c_{n0}^2 k^4 + \omega^4 - (c_{c0}^2 + v_{Ac0}^2) k^2 \omega (\omega - i\alpha \rho_{c0}) - i\alpha \omega^3 (\rho_{c0} + \rho_{n0}) - c_{n0}^2 k^2 \omega (\omega - i\alpha \rho_{n0}) = 0 \quad (3.20)$$

This represents two pairs of neutral sound and charges fast waves, as expected, modified by momentum coupling terms proportional to α . The above Eq. 3.20 is exactly Eq. (56) from Popescu Braileanu et al. (2019), where the terms related to stratification $b_n = b_c = 0$.

(b) The case of purely parallel propagation

Assuming parallel propagation $k \equiv k_{\parallel}$ to the magnetic field ($\theta = 0$), the 9th order dispersion relation can be factorized into a term which represents the Alfvén branch:

$$B_0^2 k^2 (\omega - i\alpha\rho_{c0}) - \omega^2 \rho_{c0} [\omega - i\alpha(\rho_{c0} + \rho_{n0})] = 0. \quad (3.21)$$

and a 6th order dispersion relation which contains the 1D sound branch. As the magnetic field does not affect significantly the behaviour of the thermal mode (Field, 1965), we will see that this simplification is a very good approximation. We will consider further some limiting cases and compare the results to others existing in the literature.

• No RC

When RC is not taken into account, the root $\omega = 0$, corresponding to the charges entropy mode, appears in the 6th order dispersion relation, and the remaining 5th order dispersion relation of the sound branch for parallel propagation becomes:

$$\begin{aligned} & c_{c0}^2 k^2 \left[2c_{n0}^2 k^2 \omega - 2\omega^3 - i\alpha k^2 p_{c0} + 4i\alpha\omega^2 \rho_{c0} + \alpha^2 \omega \rho_{c0} (2\rho_{c0} + \rho_{n0}) \right] + \\ & c_{n0}^2 k^2 \left[-2\omega^3 - 2i\alpha k^2 p_{n0} + 3i\alpha\omega^2 \rho_{n0} + \alpha^2 \omega \rho_{n0} (2\rho_{c0} + \rho_{n0}) \right] + \\ & \omega^2 \left[2\omega^3 + i\alpha k^2 (p_{c0} + 2p_{n0}) - i\alpha\omega^2 (4\rho_{c0} + 3\rho_{n0}) - \alpha^2 \omega (2\rho_{c0}^2 + 3\rho_{c0}\rho_{n0} + \rho_{n0}^2) \right] = 0 \end{aligned} \quad (3.22)$$

When the ion-neutral coupling is taken into account only in the momentum equation, there is another root $\omega = 0$ and the remaining 4th order dispersion relation

$$c_{c0}^2 c_{n0}^2 k^4 + \omega^4 - c_{c0}^2 k^2 \omega (\omega - i\alpha\rho_{c0}) - i\alpha\omega^3 (\rho_{c0} + \rho_{n0}) - c_{n0}^2 k^2 \omega (\omega - i\alpha\rho_{n0}) = 0. \quad (3.23)$$

represents the two pairs (neutrals and charges) of sound waves. We can observe how Eq. (3.23) is similar to the above Eq. (3.21), the only difference being that the charges sound speed was replaced by the fast magneto-acoustic speed. The above equation is identical to Eq. (31) from Popescu Braileanu et al. (2019).

• Limits depending on coupling regime

In the weak coupling regime ($\alpha \rightarrow 0$), the two-fluid 1D sound branch dispersion relation is still 6th order, but now there is a trivial root $\omega = 0$, and the neutral sound branch, unaffected by the RC decouples into

$$\omega^2 - k^2 c_{n0}^2 = 0, \quad (3.24)$$

and the remaining equation of 3rd order, when we replace $\omega = -in$, so that we get a third order polynomial equation with real coefficients, which has exact analytic solutions, becomes:

$$n^3 + a_2 n^2 + a_1 n + a_0 = 0. \quad (3.25)$$

Using the fact that the equilibrium temperature for neutrals and charges is the same, equal to T_0 , the coefficients a_0 , a_1 and a_2 can be written as:

$$\begin{aligned} a_2 &= (\gamma - 1) \rho_{c0}^2 \frac{\partial \Lambda_0}{\partial T} T_0 \frac{1}{p_{c0}}, \\ a_1 &= k^2 c_{c0}^2, \\ a_0 &= (\gamma - 1) k^2 \rho_{c0} \left[\frac{\partial \Lambda_0}{\partial T} T_0 - 2\Lambda_0 \right], \end{aligned} \quad (3.26)$$

being identical to Eq. (15) in Field (1965), if we neglect the thermal conductivity effects and we further replace $\frac{\partial \Lambda_0}{\partial T} = \frac{\mathcal{L}_T}{\rho c_0}$ and $\Lambda_0 = \frac{1}{2} \mathcal{L}_\rho$ (the factor 2 comes from considering the constant heating function).

For strong coupling regime ($\alpha \rightarrow \infty$), the higher order terms in the 6th order dispersion relation for parallel propagation disappear, and after removing a root $\omega = 0$, a third order dispersion relation remains, Eq. (3.25), but with different coefficients:

$$\begin{aligned} a_2 &= (\gamma - 1) \rho_{c0}^2 \frac{\partial \Lambda_0}{\partial T} T_0 \frac{1}{p_0}, \\ a_1 &= k^2 c_0^2, \\ a_0 &= (\gamma - 1) k^2 \rho_{c0} \left[\frac{\partial \Lambda_0}{\partial T} T_0 - 2\Lambda_0 \right] \frac{\rho_{c0}}{\rho_0}, \end{aligned} \quad (3.27)$$

where p_0 , ρ_0 , and c_0 are the pressure, density, and sound speed of the total fluid, therefore being consistent with those shown in Eqs. (3.26). In order to analyze the properties of the solutions for both cases, similarly to the derivation in Field (1965), we can further apply the following transformations:

$$\begin{aligned} y &= \frac{n}{k c_{c0}}, \\ \sigma_T &= \frac{(\gamma - 1) \rho_{c0}}{2k c_{c0}} \frac{\partial \Lambda_0}{\partial T}, \\ \sigma_\rho &= \frac{(\gamma - 1) \rho_{c0}}{2k c_{c0} T_0} (2\Lambda_0), \end{aligned} \quad (3.28)$$

for $\alpha \rightarrow 0$, and

$$\begin{aligned} y &= \frac{n}{k c_0}, \\ \sigma_T &= \frac{(\gamma - 1) \rho_{c0}}{2k c_0} \frac{\partial \Lambda_0}{\partial T} \frac{p_{c0}}{p_0}, \\ \sigma_\rho &= \frac{(\gamma - 1) \rho_{c0}}{2k c_0 T_0} (2\Lambda_0) \frac{p_{c0}}{p_0}, \end{aligned} \quad (3.29)$$

for $\alpha \rightarrow \infty$. The factor 2 in front of Λ_0 in the definition of σ_ρ comes from having a constant heating function, i.e. having the radiative cooling contribution as from Eq. (2.6), rather than Eq. (2.5).

σ_T and σ_ρ are slightly different for the $\alpha \rightarrow \infty$ compared to the $\alpha \rightarrow 0$ case, being multiplied by a factor of $\frac{p_{c0}}{p_0}$ and using the definition of the sound speed of the total fluid. With these transformations we get an equation identical to Eq. (18) in Field (1965) for both the case $\alpha \rightarrow 0$ and $\alpha \rightarrow \infty$, so that we can apply directly the same stability analysis.

Since the coefficients σ_T and σ_ρ defined in Eq. (3.29) for the strong coupling regime are proportional to those defined in Eq. (3.28) for the weak coupling regime, the conditions to have one real positive root and two complex conjugate roots with negative real part (meaning growth for the thermal mode and damping for the two propagating sound waves) are identical for both regimes and are the isobaric criterium for instability and the isentropic criterium for stability, defined by Eqs. (23) and (24) in Field (1965):

$$\begin{aligned} \sigma_T - \sigma_\rho &< 0, \\ \sigma_T + \frac{1}{\gamma - 1} \sigma_\rho &> 0, \end{aligned} \quad (3.30)$$

which become, after replacing σ_T and σ_ρ :

$$\begin{aligned} T_0 \frac{\partial \Lambda_0}{\partial T} - 2\Lambda_0 &< 0, \\ T_0 \frac{\partial \Lambda_0}{\partial T} + \frac{2}{\gamma - 1} \Lambda_0 &> 0, \end{aligned} \quad (3.31)$$

for both coupling regimes. The only difference is the factor 2 in front of Λ_0 which comes from having the constant heating function as already mentioned.

The growth of the thermal mode and the damping of the sound waves in the high k (short wavelength) regime can be approximated as the real part of the leading term of Eq. (30) in Field (1965),

$$\tilde{g} = \frac{\sigma_\rho - \sigma_T}{\gamma}, \quad (3.32)$$

$$\tilde{\delta} = \frac{\sigma_\rho + (\gamma - 1)\sigma_T}{2\gamma}. \quad (3.33)$$

The growth rate of the thermal mode goes to zero when $k \rightarrow 0$, except for the case when $\sigma_T < 0$ (Field, 1965). In that latter case, the growth can be approximated by the leading term in Eq. (33) from Field (1965):

$$\tilde{g}^L = -\sigma_T. \quad (3.34)$$

These are normalized values related to the y variable, defined in Eqs. (3.28) and (3.29), and in order to obtain the original values for the variable n , the values which appear in Eqs. (3.32), (3.33) and (3.34) have to be multiplied back by k and the corresponding sound speed, therefore the actual values do not depend on k . After replacing for σ_T and σ_ρ defined in Eq. (3.28), we obtain the following growth and damping rates for the weak coupling regime:

$$g_W = \frac{\gamma - 1}{2\gamma} \rho_{c0} \left[\frac{2\Lambda_0}{T_0} - \frac{\partial \Lambda_0}{\partial T} \right], \quad (3.35)$$

$$\delta_W = \frac{\gamma - 1}{4\gamma} \rho_{c0} \left[\frac{2\Lambda_0}{T_0} + (\gamma - 1) \frac{\partial \Lambda_0}{\partial T} \right], \quad (3.36)$$

$$g_W^L = -\frac{\partial \Lambda_0}{\partial T} \frac{\gamma - 1}{2} \rho_{c0}. \quad (3.37)$$

The growth and the damping for the strong coupling regimes are the same as those obtained in the weak coupling regime, multiplied by the factor $\frac{p_{c0}}{p_0}$:

$$g_S = g_W \frac{p_{c0}}{p_0}, \quad (3.38)$$

$$\delta_S = \delta_W \frac{p_{c0}}{p_0}, \quad (3.39)$$

$$g_S^L = g_W^L \frac{p_{c0}}{p_0}. \quad (3.40)$$

Therefore, when RC effects are added in a two-fluid model, the presence of the neutrals, sufficiently coupled to the charged particles by collisions, inhibits the growth of the thermal mode and reduces the damping on the sound waves by the same factor $\frac{p_{c0}}{p_0}$.

The constant heating function instead of the time-varying heating function usually considered, modifies slightly the isobaric and isentropic criterium, for having growth for the thermal mode and damping on the sound waves, making them easier to be fulfilled. The growth rates and the damping rates are also slightly increased.

(c) Analysis of the dispersion relation

We will now consider a general case, when the propagation is not parallel to the magnetic field, and we will solve numerically the dispersion relation. Solving the dispersion relation numerically does not give insight on the generality of the results as a purely analytic result, however, it gives accurate results when analytic methods are not possible. We can test the applicability of the analytical results obtained in limiting cases, presented previously, for this general case.

We will consider the same setup as we use later in the numerical simulations. The setup is 2D, having the magnetic field angle to the direction of propagation $\theta = 45^\circ$. Therefore we

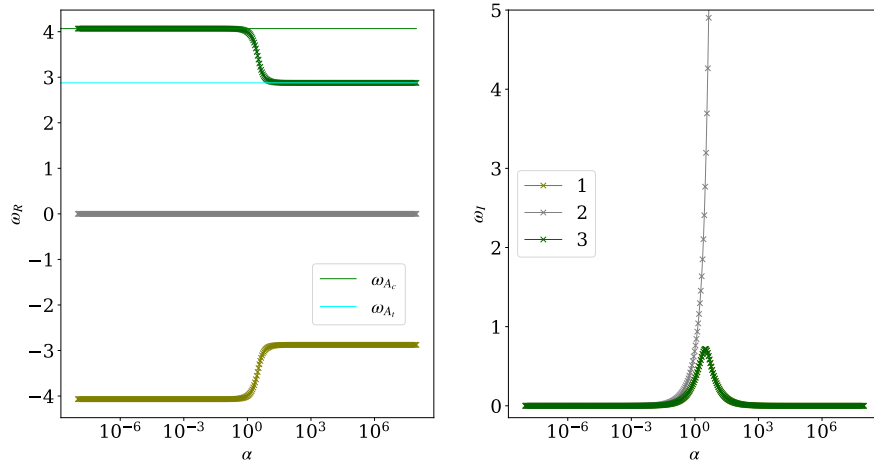


Figure 1. The three solutions of the (cubic) Alfvén branch, Eq. 3.17. The Alfvén frequencies are shown in the left panel by horizontal lines calculated as $\omega_{A_c} = v_{Ac0}k_{||}$, and $\omega_{A_t} = v_{At0}k_{||}$, with the charged fluid and total fluid Alfvén speeds, defined in Eqs. (3.6) and (3.7), respectively. We clearly recover the expected limit behavior in weak and strong coupling regimes.

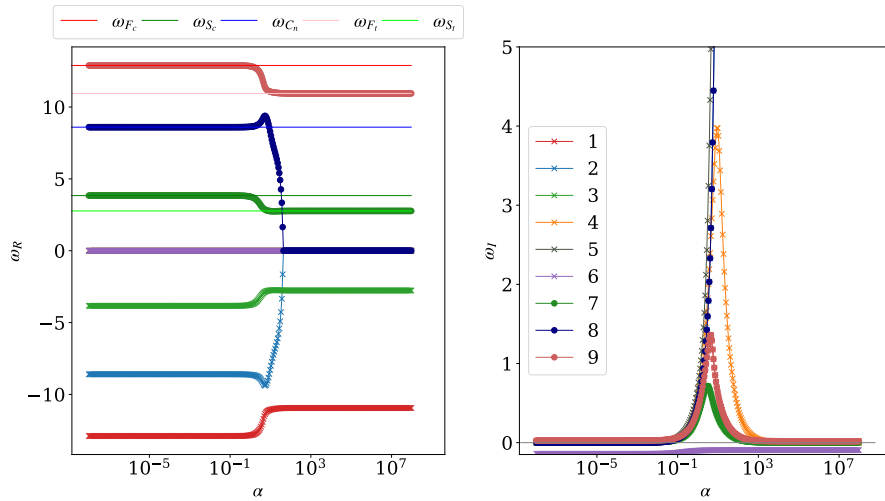


Figure 2. The nine solutions of the 9th order term, containing six propagating modes: #1, #9 fast (red); #2, #8 neutral sound (blue); #3, #7 slow (green, 'x' and 'o' for different directions); and three evanescent modes: #4 neutral entropy (orange, 'x'), #5 neutral shear (black, 'x'), #6 entropy (violet, 'x'). The evanescent modes have $\omega_R = 0$, therefore the three corresponding curves (orange, black and violet) overlap in the left panel. The frequencies shown in the left panel by horizontal lines are calculated as $\omega_{F_c} = f_{c0}k$, $\omega_{S_c} = s_{c0}k$, $\omega_{C_n} = c_{n0}k$, $\omega_{F_t} = f_{t0}k$, $\omega_{S_t} = s_{t0}k$, with the characteristic speeds f_{c0} , s_{c0} , c_{n0} , f_{t0} , s_{t0} defined in Eqs. (3.8), (3.9), (3.3), (3.9), (3.11), respectively. In the right panel an horizontal black thin line $\omega_I = 0$ is shown for clarity. Once more, limits at weak and strong coupling are fully understood.

Table 1. Units.

Quantity	Unit
length	$U_L = 10 \text{ Mm}$
number density	$U_n = 10^9 / \text{cm}^3$
temperature	$U_T = 10^6 \text{ K}$
time	$U_t = 110.1 \text{ s}$
velocity	$U_v = 90.85 \text{ km/s}$
pressure	$U_p = 0.138 \text{ dyn/cm}^2$
density	$U_\rho = 1.67 \times 10^{-15} \text{ g/cm}^3$
magnetic field	$U_B = 1.32 \text{ G}$

have to consider the dispersion relation of 9th order which describes the compressible branch in the general case, with no assumption about the angle θ . Eqs. (3.13) are written in a non-dimensional form and we used the units shown in Table 1. We consider a total background density and pressure $\rho_0 = 1.375$ and $p_0 = 2.318$, respectively. The background temperature is around 10^6 K , the parameters being characteristic for coronal plasma. As previously mentioned, the inelastic processes are not taken into account in this part. The scale height corresponding to this temperature is about 154 Mm for the neutrals and twice for the charges, therefore our domain of 10 Mm is much smaller than the scale height and the uniform medium is a good approximation. We use the cooling curve “ColganDM” (see Hermans, J., Keppens, R., 2021), unless stated otherwise. The neutral and charged densities and pressures depend on the ionization fraction ξ_i so that the temperatures of the two fluids are equal, and for Hydrogen only and charge neutrality:

$$\begin{aligned} \rho_{c0} &= \xi_i \rho_0, & \rho_{n0} &= (1 - \xi_i) \rho_0, \\ p_{c0} &= p_0 \frac{2\xi_i}{1 + \xi_i}, & p_{n0} &= p_0 \frac{1 - \xi_i}{1 + \xi_i}, & T_{c0} &= T_{n0} = T_0 = \frac{p_0}{\rho_0} \frac{1}{1 + \xi_i}. \end{aligned} \quad (3.41)$$

We will show next the 12 solutions for ω to the general 3D system of Eqs. (3.13). For the parameters considered in our case, both conditions from Eqs. (3.30) are satisfied, meaning that the thermal mode grows and the sound waves are damped. In the low plasma β regime, which is the case of the solar corona, the propagation speed of the slow waves in the charged fluid is approximately equal to the sound speed of the neutrals for the angle $\theta = 45^\circ$ considered. Therefore we considered for this plot a case with relatively high plasma $\beta \approx 2$ for a better visualization. We considered $\xi_i = 0.5$, $B_0 = 0.76$ and the mode number $n_w = 1$. The mode number n_w is related to the wave number k as $k = 2\pi n_w / L$, where L is the length of the domain. Therefore the wave number is $k = 2\pi$, for $n_w = 1$ and a domain length equal to 1.

Figure 1 shows the solutions of the Alfvén branch. The plots show the real and the imaginary part of the wave temporal frequency ω as a function of the collisional parameter α . The real part of the temporal frequency is related to the propagation speed and the imaginary part to changes of the amplitude, a negative value means growth, while a positive value means damping. There are two propagating modes ($\omega_R \neq 0$), being the Alfvén waves propagating in both directions with a speed corresponding to the Alfvén speed calculated using charged fluid properties for small α and using the total fluid properties for large α . The Alfvén waves have maximum damping for intermediate coupling ($\omega_R \approx \alpha \rho_0$). The third solution in this cubic branch is an evanescent wave ($\omega_R = 0$), which is strongly damped for increasing α . These waves were studied in detail by Soler et al. (2013a).

Figure 2 shows the solutions of the 9th order dispersion relation corresponding to the compressible branch. The magneto-acoustic waves were studied by Soler et al. (2013b). We identify six solutions corresponding to propagating waves, in pairs for the two propagation directions and three evanescent modes. The three pairs of propagating modes are the neutral sound, and the charges fast and slow waves. For weak coupling ($\alpha \rightarrow 0$) the propagation speed of

the fast and slow modes correspond to the charged fluid properties (f_{c0} and s_{c0} , from Eqs. (3.8) and (3.10), respectively) and become the propagation speed for the total fluid (f_{t0} and s_{t0} , defined in Eqs. (3.9) and (3.11), respectively) as the coupling increases. When the coupling increases, the neutral sound mode becomes damped (the imaginary part is positive and increases). We can also observe that the damping of the Alfvén wave is similar to the damping of the slow wave (the slow wave has Alfvénic properties, with motions almost perpendicular to the field lines, in high β plasma regime). The Alfvén wave damping is smaller than the damping of the fast wave and the neutral wave.

The largest damping of the three evanescent modes (corresponding to solution #5), increasing with increasing α , is very similar to that found for the evanescent wave on the Alfvén branch (solution #2 in Figure 1). In order to understand if the dynamics of the mode is dominated by the magnetic forces or the plasma pressure gradient we can choose an eigenvalue on the curve and look at the eigenvector associated to it, which contains the amplitudes of the variables. We choose the eigenvalues corresponding to $\alpha = 10^2$ (strong coupling) and $\alpha = 10^{-6}$ (weak coupling). The eigenvalues and eigenvectors for these two cases and for the two branches are shown in the Appendix 7. We can observe that for the mode corresponding to solution #5, in the weak coupling case, the perturbation is mostly in the velocity of the neutrals in the direction perpendicular to \mathbf{k} , thus, this mode should be called the neutral shear wave. The properties of this mode are indeed similar to those of the evanescent mode on the Alfvén branch. In the strong coupling regime, both neutrals and charges oscillate in the direction perpendicular to \mathbf{k} in high beta plasma regime (as shown in these Figures) or almost along the field lines in low beta plasma regime ($B_0 = 10$), keeping the total momentum constant.

The mode corresponding to solution #4 is mostly damped for intermediate coupling. For the weak coupling regime the perturbation is mostly for the density of the neutrals, thus this mode is the neutral entropy mode. In the strong coupling regime, there are perturbations in the densities and pressures of neutrals and charges, so that the total pressure is kept constant and the temperature perturbation is the same in neutrals and charges.

The mode corresponding to solution #6 is the only one which is growing ($\omega_I < 0$). In the weak coupling regime, the perturbation is mostly in the charged fluid density, therefore this is called the (charges) entropy mode or the thermal mode. When the cooling term is not included in the equations, the thermal mode does not grow, having $\omega = 0$. In the strong coupling regime, the perturbation is mostly in the densities of neutrals and charges, with an amplitude ratio equal to the ratio of the background densities. The perturbations are almost isobaric, similarly to the single-fluid case (Field, 1965).

The radiative cooling also produces damping on the slow and fast modes, but this is much smaller than the damping produced by collisions for intermediate coupling regime and cannot be distinguished visually in the plots. For both solutions #4 and #6 the magnetic field is only slightly perturbed, creating even smaller perturbations in the velocity, aligned with the magnetic field, as in the single-fluid case (Field, 1965). As these perturbations in the magnetic field and velocity are orders of magnitude smaller than those in density we can conclude that the linear evolution of the modes corresponding to solutions #4 and #6 is not determined by the magnetic field.

Figure 3 shows the imaginary part of the thermal mode as a function of the collisional parameter α for several values of the ionization fraction. The values of the background atmosphere depend on the ionization fraction as in Eqs. (3.41), therefore a higher ionization fraction means a higher density and lower temperature for the charged fluid. For the cooling curve used here, the radiative cooling effects are larger for smaller temperatures around the equilibrium value. Therefore the growth rate is increased for higher ionization fraction because of two effects: lower temperature and higher density in the charged fluid. The ratio between the growth of the thermal mode in the high coupling regime and the weak coupling regime depends on the ionization fraction only: $\frac{p_{c0}}{p_0} = \frac{2\xi_i}{1+\xi_i}$. The limits for weak and strong coupling, as defined in Eqs. (3.35) and (3.38), respectively, are shown by thin, horizontal lines. We can see a perfect agreement, therefore the single-fluid analysis through the weak and strong coupling limiting

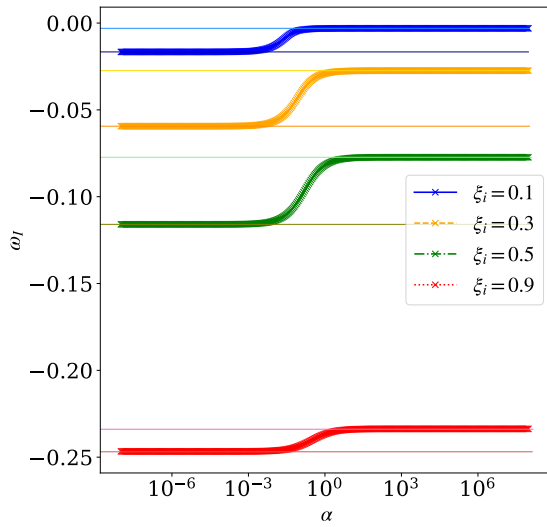


Figure 3. Thermal mode growth as a function of the collisional parameter α for different ionization fractions. The thin horizontal lines show the analytical growth rates obtained from Eq. (3.35) for $\alpha \rightarrow 0$ and Eq. (3.38) for $\alpha \rightarrow \infty$.

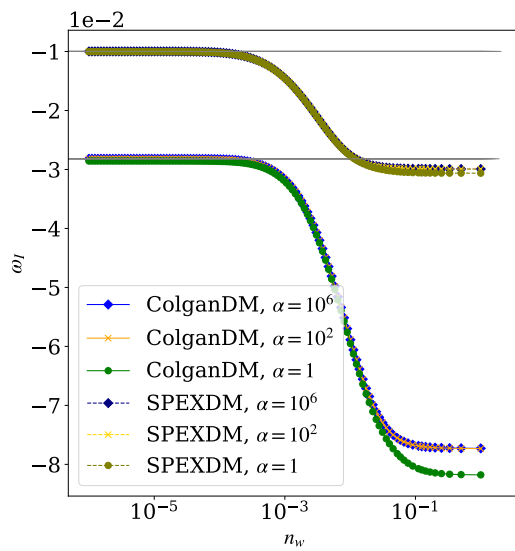


Figure 4. Growth of the thermal mode as a function of the mode number $n_w = \frac{1}{m}$, with m with integer values from 1 to 10^6 . The fractional mode number corresponds to scales larger than the length of the domain, having $k = 2\pi n_w$. We compare two cooling functions “ColganDM” (marked with “x”) and “SPEXDM” (marked with “o”) and three values for the collisional parameter α indicated by three different colors. The horizontal black lines show the analytical growth rates calculated in the high coupling regime for the $k \rightarrow 0$ limit, as from Eq. (3.40), for both curves.

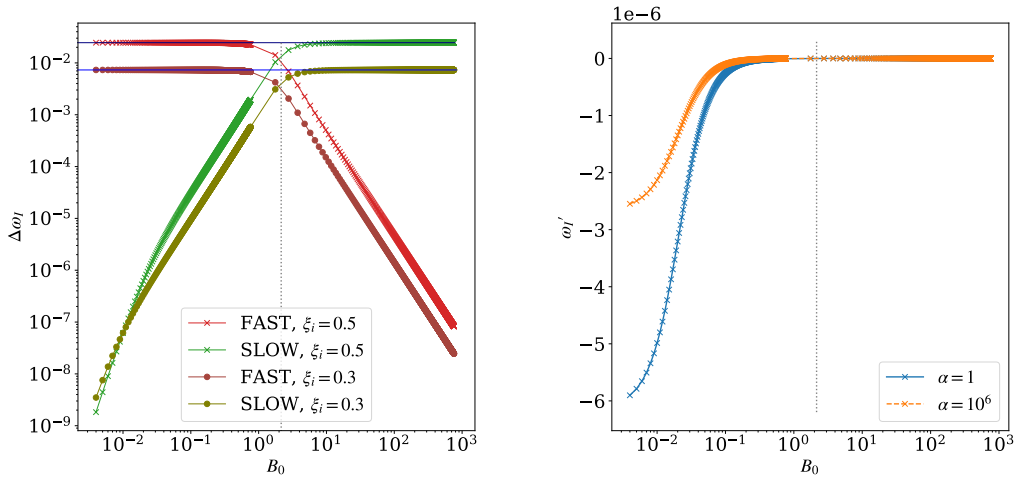


Figure 5. The dependence on the magnetic field magnitude. Left: Damping due to radiative losses $\Delta\omega_I = \omega_I - (\omega_I)_{\text{noRC}}$ for fast (green) and slow (red) modes, for the strongly coupled case $\alpha = 10^6$. The horizontal blue lines show the damping of the 1D sound mode in high coupling regime as from Eq. (3.39). Right: Imaginary part of the thermal mode compared to the low beta limit growth: $\omega_I' = \omega_I - (\omega_I)_{B_0=758}$. The low beta limit of the imaginary part $(\omega_I)_{B_0=758}$ was subtracted for a better visualization because it has values which are four orders of magnitude larger: $(\omega_I)_{B_0=758, \alpha=1} = -0.082$ and $(\omega_I)_{B_0=758, \alpha=10^6} = -0.077$. The ionization fraction considered was $\xi_i = 0.5$ and the mode number $n = 1$. The dotted vertical gray line shows the equipartition value $\sqrt{\gamma p_0}$ in both panels.

cases gives an almost complete description of the thermal mode growth in the two-fluid model. Those limits are obtained for the high wavenumber k regime, indicating that the length of our domain is a small scale for the cooling effects.

Figure 4 shows the imaginary part of the thermal mode as a function of the mode number n_w . In the previous figure we considered $n_w = 1$, and the limits obtained for high k regime gave very good matching, indicating that the scale corresponding to the domain length is a small scale for the radiative cooling effects. Therefore, we considered scales from $m = 1$ up to $m = 10^6$ larger than our domain, having the fractional mode number $n_w = \frac{1}{m}$. We compared two different cooling functions “ColganDM” and “SPEXDM” (see also Hermans, J., Keppens, R., 2021) and three values of the collisional parameter α . We can observe that for both cooling functions the curves for different collisional parameters α converge to the same value as $k \rightarrow 0$; the collisional mean free path becomes smaller than the infinitely large scale associated to k , regardless the value of α . The growth rates for the “SPEXDM” curve are smaller than for the “ColganDM” curve, being consistent with the results of the simulations presented in Hermans, J., Keppens, R. (2021). The asymptotic value of the growth for the “ColganDM” cooling function at $n = 1$ (corresponding to the high k regime) is consistent to the values seen in Figure 3 for $\xi_i = 0.5$ and the corresponding value of α . For the parameters considered here, $\frac{\partial A_0}{\partial T} < 0$, therefore we can calculate the analytical growth rate for $k \rightarrow 0$ case using Eq. (3.40), corresponding to the high coupling regime, since $k \rightarrow 0$ is the infinite coupling limit in the two-fluid model, seen as well in the convergence of the curves for different α to the same limit when $k \rightarrow 0$. These analytical values are shown in the plot by horizontal thin black lines and we can observe a perfect agreement.

Figure 5 shows the effect of radiative losses on the damping of slow and fast waves (left panel) and the imaginary part of the thermal mode (right panel) when we vary the magnitude of the magnetic field. We can observe smaller damping around the equipartition field, where the waves have mixed sound and magnetic properties. At the equipartition point, the fast mode transforms

from having sound wave properties (isotropic, motion mostly along the direction of propagation for high β regime) to Alfvénic wave (motion almost perpendicular to the magnetic field) and the slow mode transforms from an Alfvénic wave to a sound wave (motion mostly along the field lines for low plasma β regime). Both of the modes are damped while having sound properties, the fast wave for fields below the equipartition layer and the slow wave for fields above and we can find perfect agreement with the analytical damping rates.

In the single-fluid assumption, the magnetic field has no effect on the linear evolution of the thermal mode if $\mathbf{k} \parallel \mathbf{B}$. When $\mathbf{k} \perp \mathbf{B}$, the growth is inhibited because of the increase of magnetic pressure in the condensed regions because the field is frozen into the plasma (Field, 1965). We can observe in the right panel of Figure 5 that, indeed, the influence of the magnetic field to inhibit the growth is very small, the difference in the growth for a large change in the magnetic field is four orders of magnitude smaller than the values of the growth for both coupling regimes.

4. Simulations

In order to better compare the effect of radiative cooling in the two-fluid to the single fluid model in numerical simulations, we will consider the same setup and uniform background values as in Claes, Keppens (2019); Hermans, J., Keppens, R. (2021), where a uniform periodic 2D box is perturbed by (damped) magnetosonic waves that ultimately give way to the thermal instability which causes a condensation to form.

The 2D domain used in the simulations has length equal to 1 in both dimensions. We used periodic boundary conditions. The magnetic field is oriented by an angle of 45° , with respect to the x -direction, $B_{x0} = B_{z0} = B_0/\sqrt{2}$. We use the same values used in the previous section for the background variables and $k = 2\pi$. The perturbation is initially a superposition of two single-fluid slow waves, with the same parameters, but different propagation angles of 45° and -45° , with respect to the magnetic field, described by:

$$v_{cz} = V_1 \cos(kz) + V_2 \cos(kx), \quad (4.1)$$

$$v_{nz} = V_1 \cos(kz) + V_2 \cos(kx), \quad (4.2)$$

$$v_{cx} = V_2 \cos(kz) + V_1 \cos(kx), \quad (4.3)$$

$$v_{nx} = V_2 \cos(kz) + V_1 \cos(kx), \quad (4.4)$$

$$B_{x1} = B_1 \cos(kz), \quad (4.5)$$

$$B_{z1} = B_1 \cos(kx), \quad (4.6)$$

$$p_{c1} = P_1 \frac{\rho_{c0}}{\rho_0} (\cos(kz) + \cos(kx)), \quad (4.7)$$

$$p_{n1} = P_1 \frac{\rho_{n0}}{\rho_0} (\cos(kz) + \cos(kx)), \quad (4.8)$$

$$\rho_{c1} = R_1 \frac{\rho_{c0}}{\rho_0} (\cos(kz) + \cos(kx)), \quad (4.9)$$

$$\rho_{n1} = R_1 \frac{\rho_{n0}}{\rho_0} (\cos(kz) + \cos(kx)). \quad (4.10)$$

Table 2. Parameters of the simulations.

Number	ξ_i	α	B_0	Plasma β	Name
1	0.3	10^6	0.76	2	I1- α 3-B1
2	0.5	10^6	0.76	2	I2- α 3-B1
3	0.5	10^6	7.6	0.02	I2- α 3-B2
4	0.5	1	7.6	0.02	I2- α 1-B2
5	0.5	10^2	7.6	0.02	I2- α 2-B2
6	0.9	10^2	7.6	0.02	I3- α 2-B2
7	0.9	10^2	0.76	2	I3- α 2-B1

Table 3. The linear growth rates calculated from the simulations, with the linear phase indicated in Figure 6, and the analytical growth rates, calculated numerically from the dispersion relation.

Name	Growth rate sim.	Growth rate an.
I1- α 3-B1	0.040 ± 0.003	0.027
I2- α 3-B1	0.166 ± 0.006	0.077
I2- α 3-B2	0.165 ± 0.003	0.077
I2- α 1-B2	0.187 ± 0.003	0.082
I2- α 2-B2	0.173 ± 0.004	0.077
I3- α 2-B2	0.482 ± 0.014	0.234
I3- α 2-B1	0.527 ± 0.014	0.234

We used the following quantities characteristic for the slow waves (Goedbloed et al., 2019):

$$\omega = ks_{t0}, \quad (4.11)$$

$$V_1 = A, \quad V_2 = \frac{B_{x0}^2 k^2}{B_{x0}^2 k^2 - \omega^2 \rho_0} V_1, \quad (4.12)$$

$$B_1 = \frac{1}{\omega} B_{x0} k (V_1 - V_2), \quad (4.13)$$

$$P_1 = \frac{1}{\omega} c_{t0}^2 k \rho_0 V_1, \quad (4.14)$$

$$R_1 = \frac{1}{\omega} k \rho_0 V_1, \quad (4.15)$$

with s_{t0} the propagation speed for the total fluid, defined in Eq. (3.11). We chose the amplitude $A = 10^{-3}$.

We used the same (physical) values for density ρ_0 and pressure p_0 , split according to the specified ionization fraction ξ_i into neutral and charged fluids, as described in Eqs. (3.41), in order to have the same temperature for neutrals and charges. We used two different values for the magnetic field magnitude with physical values of 1 G and 10 G, and we also varied the collisional parameter α and the ionization fraction ξ_i , as shown in Table 2.

Figure 6 shows the evolution of the maximum of the perturbation in the density of charges as a function of time. The linear growth rates calculated from the simulations and the analytical ones, obtained from solving numerically the 9th order dispersion relation are shown in Table 3. We can observe systematically for the seven simulations that the analytical results presented earlier are verified. The largest difference in the curves is given by changing the ionization fraction. Larger ionization fraction means larger growth, and this is consistent with Figure 3. The difference for changing the ionization fraction is larger than other effects, therefore we observe that the seven curves are grouped by this parameter. Within the groups, the growth rates are further ordered depending on the collisional parameter α , smaller α meaning larger growth. Changing the

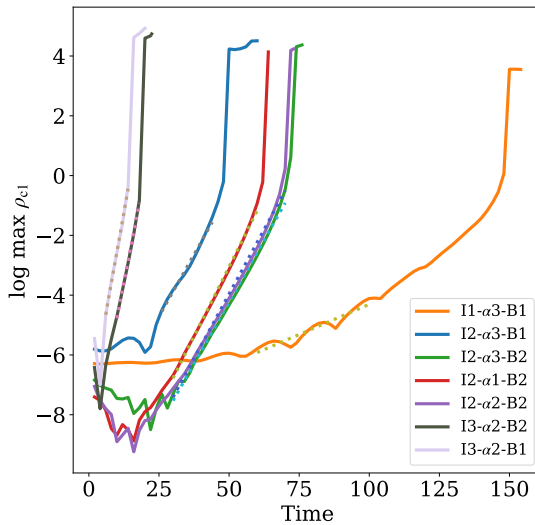


Figure 6. Time evolution of the logarithmic value of the maximum density of the charged fluid for the seven simulations shown in Table 2. The linear growth rates can be calculated as the slopes of the curves during the linear phase. The interval of time fitted for the linear phase is shown with dotted lines. The values of the fit and the errors as well as the analytical growth rates are shown below for each of the simulations in Table 3.

magnetic field magnitude has no significant effect on the growth rate. There are small differences at the beginning because we do not excite exact eigenmodes with the same amplitude. We use the same perturbation in all the simulations (the same as in Hermans, J., Keppens, R., 2021), representing single-fluid ideal MHD slow modes which are not eigenmodes of our system. The growth of the thermal mode can be seen after the slow waves are damped, therefore it is difficult to calculate precisely the linear growth rates from the simulations. However, in the case when $\xi_i = 0.3$, the growth of the thermal mode is much smaller than in the other cases; the damping rate is also smaller, but by a smaller factor (see Figures 3 and 5). For this case, the calculated linear growth rate as the slope of the linear fit corresponds almost exactly to the analytical value. When the growth rates are larger, it is more difficult to separate the linear phase to the nonlinear phase and the linear fit is not precise anymore, as we can see that the values obtained from the simulations deviate from the analytical growth rates for the larger ionization rates of 0.5 and 0.9, by a factor of almost two in the latter case. This is considered a very good agreement to the analytic predictions, given the way we initialize the simulations; the ordering between the values is kept, and overall, qualitatively, the simulations growth rates follow the theory.

Figure 7 shows the last snapshots of densities (columns a) and b)), temperatures (columns c) and d)) and decoupling velocity (column e)) from the simulations shown in Table 2. In the panel which shows the decoupling velocity we also show the magnetic field lines. The evolution of the thermal instability is already in the nonlinear phase, when we can observe a high density structure in the direction perpendicular to the magnetic field, in the bottom left part of the domain. The similar location of the condensation for the seven simulations might be related to the decomposition of the initial perturbation (which contains only one scale, $n_w = 1$), in the nine eigenmodes of the system, and the values of the components of the eigenvector associated with the thermal mode, which give the initial (real) amplitudes and phase shifts. It was mentioned previously that the very small velocity perturbed for the thermal mode is aligned with the magnetic field, even for very small values of the magnetic field. By superposing two initial

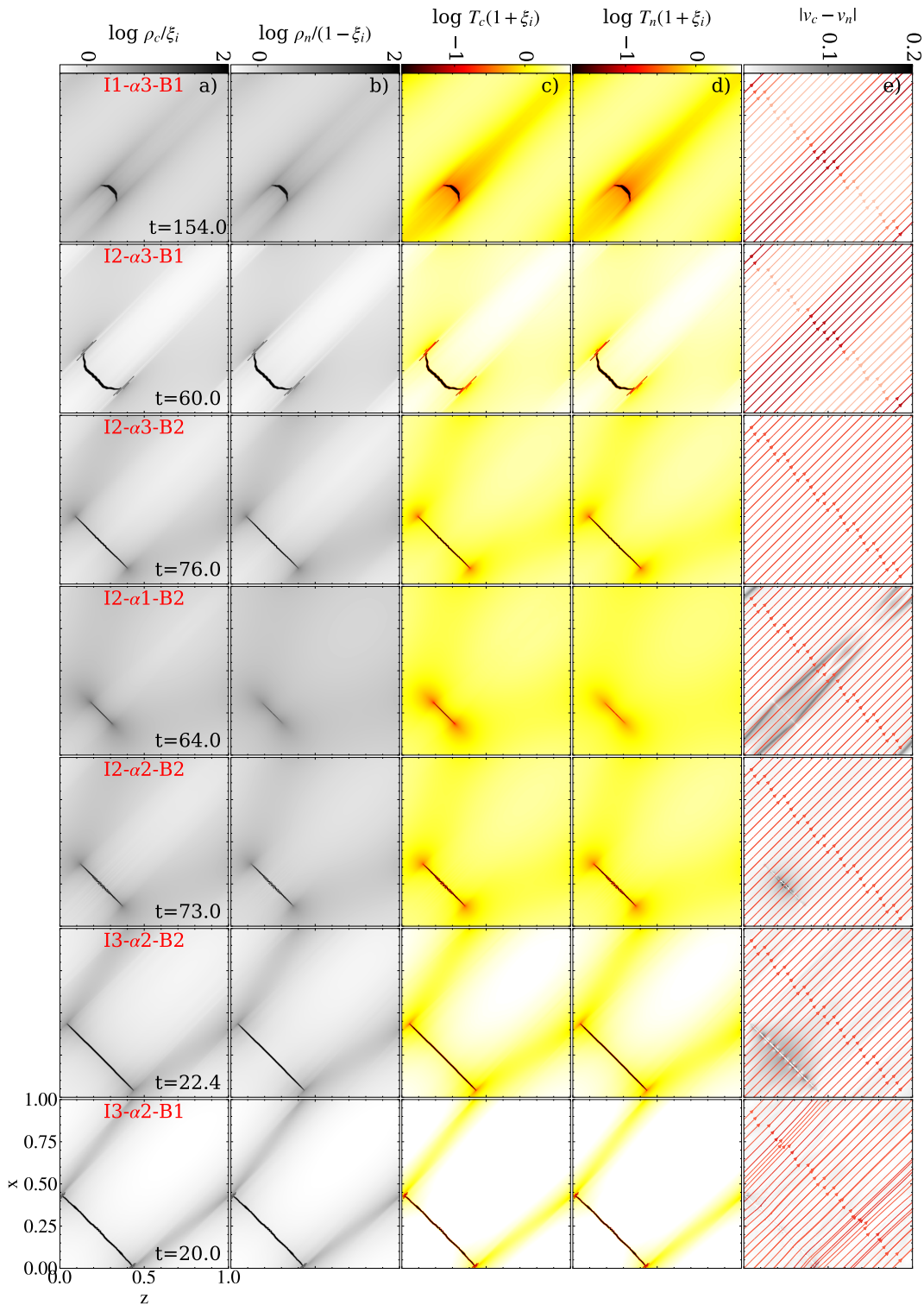


Figure 7. Last snapshots of the seven simulations shown in Table 2 shown on the seven rows. The columns correspond to different quantities: density of charges, density of neutrals, temperature of charges, temperature of neutrals, magnitude of the decoupling in the velocity. For a better visualization, in order to eliminate the effect of having different background neutral and charged densities and temperature for different ionization fractions, the quantities shown in the plots are normalized to have the background value equal to ρ_0 and the temperature p_0/ρ_0 . The magnetic field lines are overplotted in the fifth column with a red colormap, a darker color meaning a larger magnitude.

perturbations in the two dimensions (see Eqs. (4.1)-(4.10)), these velocities have opposite signs making the structure stable (Hermans, J., Keppens, R., 2021). In the nonlinear phase, the magnetic tension prevents the misalignment of the multiple scales formed later due to the nonlinear interaction. Smaller value for the magnetic field implies larger velocities as the magnetic field lines are easier to be compressed. This is because of the velocity perpendicular to the field created by the gradient in the direction perpendicular to the field of the velocity parallel to the field. This can be seen in the compressed field lines seen in the panels corresponding to the smaller field B1. In the panel I3- α 2-B1, we can observe that the magnetic tension plays a role as well.

Larger ionization fraction produces larger structures as we can see by comparing the pairs I1- α 3-B1, I2- α 3-B1 and I2- α 2-B2, I3- α 2-B2. We can observe that for the simulations I1- α 3-B1, I2- α 3-B1 and I3- α 2-B1 the condensation starts to be slightly misaligned to the perpendicular direction to the magnetic field. The stronger magnetic tension prevents the misalignment for the other cases. We can also observe that the condensation is larger for larger ionization fraction, but this might be due to the fact that the growth is larger. Lower values of α makes the structures more diffusive and are also associated to larger values in the decoupling velocities. The low temperature structures follow mostly the high density structures and are very similar for the neutrals and the charges. In the temperature panels, we observe some regions of increased temperature at the end of the condensations, especially for smaller values of α , indicating the role of the frictional heating.

(a) Including ionization/recombination

In the simulations presented so far the ionization fraction ξ_i was an input parameter, and we varied it in order to test several regimes. However, we can calculate a realistic ionization fraction from the ionization recombination equilibrium condition for the chosen background, described by ρ_0 and p_0 . For a fixed p_0 and ρ_0 , the background temperature depends on the ionization fraction as shown in Eq. (3.41):

$$T_0 = \frac{p_0}{\rho_0(1 + \xi_i)}. \quad (4.16)$$

In order to have ionization/recombination equilibrium, the source term calculated for the background in the continuity equation must vanish. After obtaining the equilibrium temperature in eV,

$$\tilde{T} = T_0 U_T \frac{k_B}{e}, \quad (4.17)$$

where U_T is the temperature unit, defined in Table 1, and setting the continuity equations source term $S_{n0} = 0$, with the definition given in Eq. (6.1) and ionization and recombination rates from Eqs. (6.4)-(6.6), makes the ionization fraction a function of the temperature only,

$$\xi_i = \frac{\sigma^{\text{ion}}}{\sigma^{\text{ion}} + \sigma^{\text{rec}}} = f(\tilde{T}). \quad (4.18)$$

Starting with an arbitrary ionization fraction and corresponding temperature as from Eq. (4.16), we iterate over recalculating the ionization fraction using Eqs. (4.17) and (4.18), and the temperature. This procedure converges fast, in two iterations if we start with $\xi_i = 1$ and three iterations if we start with $\xi_i = 0$. We obtain the ionization fraction, corresponding to a very low fraction of neutrals, $1 - \xi_i = 1.019 \times 10^{-6}$.

The ionization/recombination and the radiative cooling processes are not independent, as part of the radiative losses are due to the recombination. We used ionization/recombination rates and cooling curves parametrized as function of temperatures and densities only, calculated in external models. These rates should be calculated consistently by the model, but this is a very difficult task to put in practice.

For the following nonlinear two-fluid simulations where we include ionization-recombination, we will change the perturbation to be similar to the thermal runaway setup shown in the demo simulations of our code MPI-AMRVAC 3.0, see Keppens et al. (2023), adapted for the two-fluid model. In practice, we set up a circular region of higher density and lower temperature

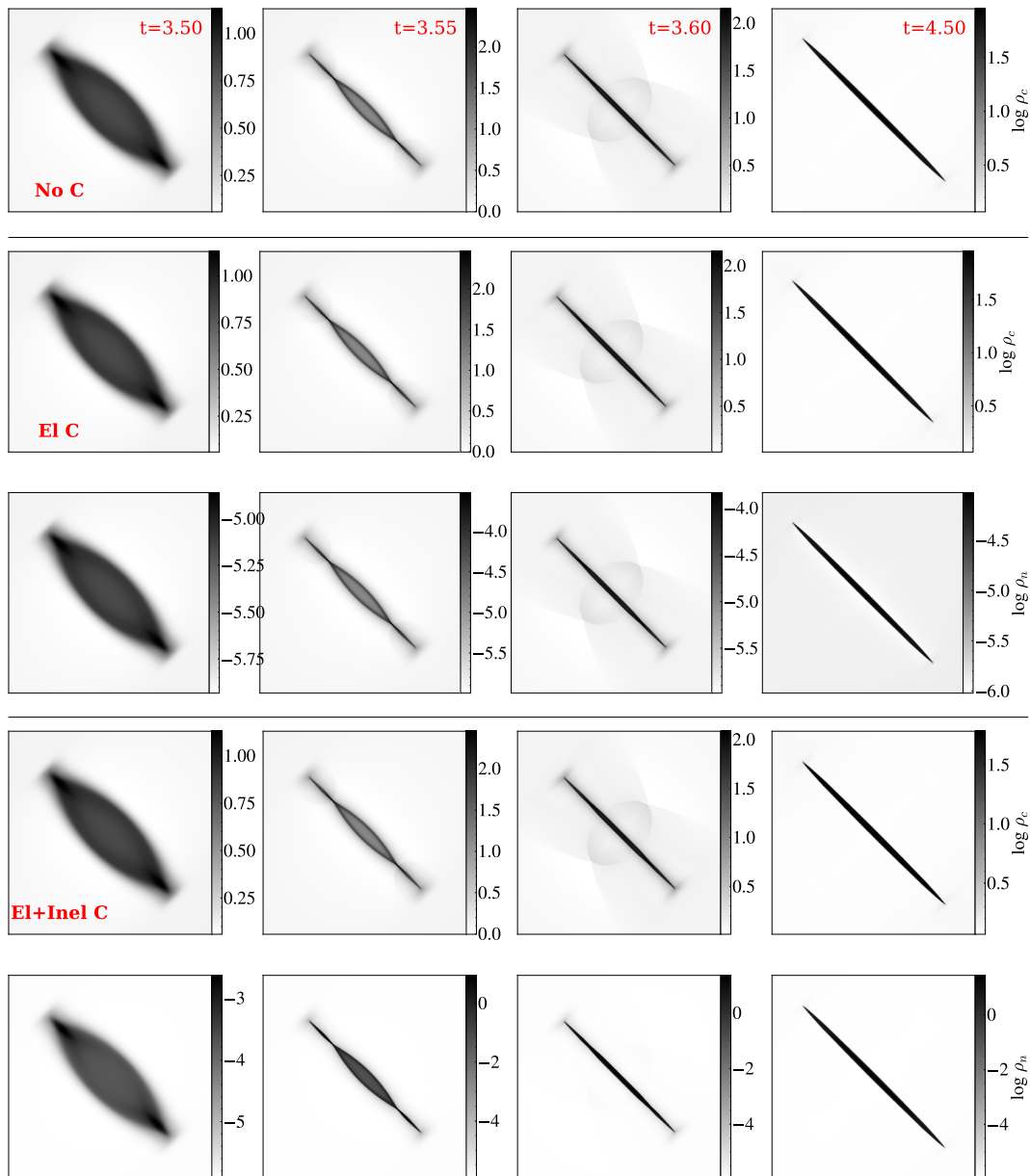


Figure 8. Time evolution of the densities for “No C”, “El C” and “El+Inel C”. For “No C” we show only the density of charges, because the neutrals do not evolve at all, since there is no coupling with the charges. The movies of the three simulations are available online.

in a uniform field and pressure. This will then evolve by thermal runaway/instability, where a condensation forms that again is oriented perpendicular to the (45°) magnetic field.

We will compare three simulations: an uncoupled case “No C” when there is no coupling between neutrals and charges, “El C” when we consider only elastic coupling and “El+Inel C” when we include ionization/recombination effects besides the elastic collisions. The value of the collisional parameter α is now calculated self-consistently, from the plasma parameters and has the non-dimensional value $\alpha \approx 10^3$, being almost constant and uniform during the simulation.

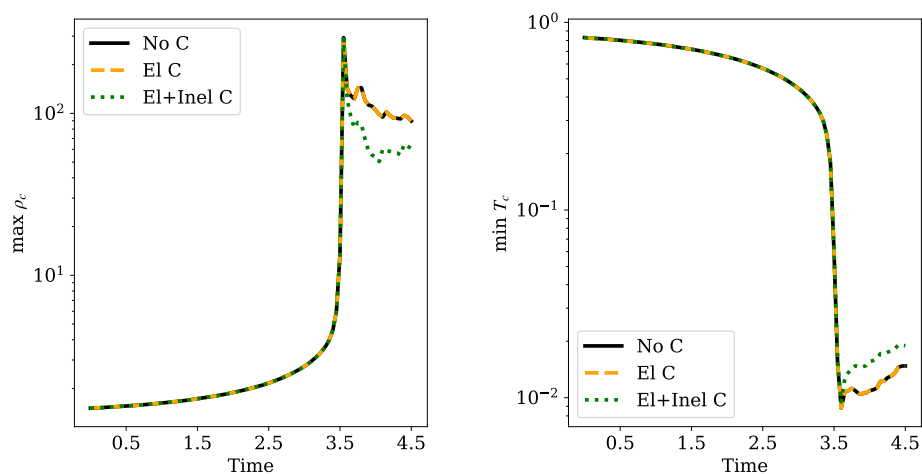


Figure 9. Evolution of the maximum density of charges as a function of time for the three simulations: “No C”, “El C” and “El+Inel C”, shown by the different curves as indicated in the legend.

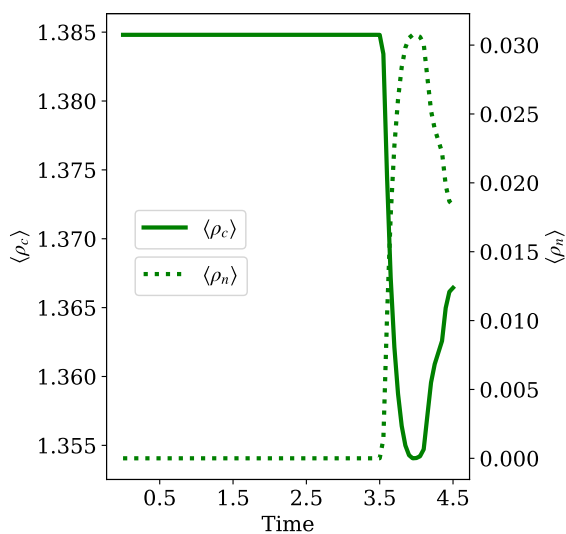


Figure 10. Evolution of the mean density of charges (solid line, left axis) and neutrals (dotted line, right axis) as a function of time in the simulation “El+Inel C”.

We show in Figure 8 the time evolution of the densities for the three cases. Visually, the structures in both densities look very similar for the three simulations, except for the “El+Inel C” case, where we see a significant larger fraction of neutrals by four orders of magnitude. After the compression stops, both neutrals and charges expand, following a rebound shock wave, seen for both charges and neutrals in the “El C” case, as it can be estimated in the panels of the third

column at time $t = 3.6$. The shock wave cannot be seen in the neutral fluid for “El+inel C”, being damped by the recombination processes.

Figure 9 shows the time evolution of the maximum of the density of charges (left panel) and the minimum temperature (right panel) of charges for the three simulations. The maximum in density is reached at the same time as the minimum in the temperature as it can be also visually estimated from Figure 8 and has similar values for the three simulations. The decrease in temperature triggers the recombination of the charges, this being the cause of the large increase in the density of neutrals.

As the temperature grows the cooling becomes active again and the plasma condensates again. There are several cycles of condensation and cooling followed by heating and expansion, seen as small oscillations in the density and temperature curves. There is an extra heating effect coming from the elastic interaction with the neutrals in the simulations “El C” and “El+inel C”, which can be slightly seen in the minimum temperature evolution. For the “El+inel C” case, after the first peak, the maximum charges density drops visibly compared to the other two cases, because of the ionization/recombination.

Figure 10 shows the time evolution of the mean density of neutrals and charges for “El+inel C”. We can observe a significant drop in the density of charges and a corresponding increase in the density of neutrals by four orders of magnitude because of the recombination. This happens after the minimum peak in temperature is reached, when the recombination rates are highest. Afterwards, when the temperature starts to increase again, the ionization effects become more important, and the density of charges starts to increase again. These heating-cooling cycles affect the ionization/recombination processes and it can be seen in the small oscillations of the mean densities.

5. Conclusions

In this paper we studied the radiative cooling effects in a two-fluid model, by adding the radiative losses in the charges energy equation. In the analytical derivation we considered a 1D case, thus discarding the effects of the magnetic field, and the limiting cases of weak and strong coupling which can be treated analytically, following the derivation in Field (1965). We find that the stability criterium for the thermal mode and for the sound waves, the isobaric and isentropic criteria, respectively, as defined in Field (1965) remain unchanged. For the parameters considered in this paper, characteristic to the solar corona, radiative cooling produces growth of the thermal mode and damping of the sound waves. We highlighted the difference between having a constant heating function instead of time-varying as considered in the analytic derivation of Field (1965). The isobaric and isentropic criterium, for growth for the thermal mode and damping of sound waves, are slightly easier to fulfill and growth and damping rates are increased when we use the constant heating function.

Radiative cooling has no effect on Alfvén waves and damps the waves with sound properties when the restoring force is the pressure gradient. We observed how the single-fluid analysis in a 1D geometry, without the magnetic field gives a very good description of the radiative loss effects. The growth of the thermal mode and damping of the waves are recovered from the single-fluid analysis for weak and strong coupling. The growth of the thermal mode and the damping of the sound waves are reduced by the presence of the neutrals in the strong coupling regime by the same factor, which depends on the ionization fraction only, $\frac{2\xi_i}{\xi_i+1}$.

The analysis of the linear equations and the simulation results showed that in our case the largest difference in the growth of the thermal mode is given by changing the ionization fraction, among changing other parameters, such as the collisional coupling regime or the magnetic field strength, because it means a change in the background atmosphere. Changing the ionization fraction means changing the background atmosphere, increasing the ionization fraction means decreasing the temperature and increasing the density of charges, therefore increasing the growth of the thermal mode and the damping on the sound waves. We also obtained larger growth rates for smaller values of the collisional parameter α . In the nonlinear phase the structures are larger

for larger ionization fraction and more diffuse for smaller values of the collisional parameter α . In this case, when α is smaller, we observe an increase in the temperature at the end of the condensed structures, which might be due to the frictional heating.

The magnetic field magnitude is not relevant for the thermal mode linear growth. The increase in the growth when the field magnitude goes to zero is four orders of magnitude smaller than the value of the growth found in very low β plasma regime. The damping on the slow and fast waves in regimes where they have sound properties coincides with the damping obtained analytically for 1D sound waves for the corresponding coupling regime. The slow waves are damped in the low plasma β regime and the fast waves are damped in the high β plasma regime. The damping is slightly smaller around the equipartition value for the magnetic field magnitude when both waves have mixed sound and magnetic properties. The magnetic field might become more important for perpendicular propagation, however these effects are small compared to the effects of the parallel conductivity (Field, 1965), which was not taken into account in this study. In the nonlinear phase, the condensed structures align perpendicularly to the magnetic field lines, as seen in the simulations by Claes, Keppens (2019); Hermans, J., Keppens, R. (2021).

The recombination of the charges when the temperature drops leads to an increase in the neutral density of four orders of magnitude. Including ionization-recombination introduced more significant effects in the evolution of the thermal instability than the elastic collisions as seen from Figures 8 and 9.

6. Appendix A: Collisional terms

$$S_n = \rho_c \Gamma^{\text{rec}} - \rho_n \Gamma^{\text{ion}}, \quad (6.1)$$

$$\mathbf{R}_n = \rho_c \mathbf{v}_c \Gamma^{\text{rec}} - \rho_n \mathbf{v}_n \Gamma^{\text{ion}} + \rho_n \rho_c \alpha (\mathbf{v}_c - \mathbf{v}_n), \quad (6.2)$$

$$\begin{aligned} M_n = & \frac{1}{2} \rho_c v_c^2 \Gamma^{\text{rec}} - \frac{1}{2} \rho_n v_n^2 \Gamma^{\text{ion}} + \frac{1}{2} (v_c^2 - v_n^2) \rho_n \rho_c \alpha \\ & + \frac{1}{\gamma - 1} (\rho_c T_c \Gamma^{\text{rec}} - \rho_n T_n \Gamma^{\text{ion}}) \\ & + \frac{1}{\gamma - 1} (T_c - T_n) \rho_n \rho_c \alpha. \end{aligned} \quad (6.3)$$

Expressions for Γ^{ion} and Γ^{rec} as functions of n_e and T_e are given in Voronov (1997) and Smimov (2003); are those described by Eqs. (A5) and (A4), respectively in Popescu Braileanu, B., Keppens, R. (2022), the same as Eqs. (A.2), (A.1) from Popescu Braileanu et al. (2019):

$$\Gamma^{\text{rec}} \approx n_e \sigma_{\text{rec}} s^{-1} \quad \Gamma^{\text{ion}} \approx n_e \sigma_{\text{ion}} s^{-1}, \quad (6.4)$$

$$\sigma^{\text{ion}} = \frac{A}{X + \frac{E_{\text{ion}}}{\tilde{T}}} \left(\frac{E_{\text{ion}}}{\tilde{T}} \right)^K \exp \left(\frac{E_{\text{ion}}}{\tilde{T}} \right), \quad \sigma^{\text{rec}} = \frac{1}{\sqrt{\tilde{T}}} (2.6 \times 10^{-19}), \quad (6.5)$$

$$(6.6)$$

\tilde{T} is the temperature in eV, $A = 2.91 \times 10^{-14} \text{ m}^3/\text{s}$, $K = 0.39$, $X = 0.232$, $E_{\text{ion}} = 13.6 \text{ eV}$.

7. Appendix B: Eigenvectors and eigenvalues

Below we show the numerical values of the eigenvalues and eigenvectors for the case $\xi_i = 0.5$, $k = 1$. For a better readability, the real and imaginary parts with absolute values smaller than $2^{-23} = 1.19e - 7$ (the float machine precision) are set to 0. Each row of the eigenvectors matrix V correspond to the eigenvalues shown in the vector Λ . The eigenvectors contains the amplitudes of: v_{cy} , v_{ny} , B_{y1} , for the Alfvén branch and p_{c1} , p_{n1} , v_{cx} , v_{nx} , v_{cz} , v_{nz} , ρ_{c1} , ρ_{n1} , B_{z1} for the compressible branch. All the calculations are done for $B_0 = 1$ (the case shown in Figures 1 and

2), except for the coupled case, where we also calculated the case $B_0 = 10$ for the compressible branch, as indicated below.

High beta regime ($B_0 = 1$)

(a) $\alpha = 10^{-6}$ (uncoupled case)

(i) Alfvén branch

$$A = \begin{bmatrix} -4.07 + 3.44e - 7i \\ 6.88e - 7i \\ 4.07 + 3.44e - 7i \end{bmatrix}$$

$$V = \begin{bmatrix} 0.77 & 1.30e - 7i & 0.64 \\ 0 & 1 & -1.40e - 7i \\ 0.77 & -1.30e - 7i & -0.64 \end{bmatrix}$$

(ii) Compressible branch

$$A = \begin{bmatrix} -12.89 + 0.03i \\ -8.60 + 4.81e - 7i \\ -3.84 + 0.0045i \\ 4.13e - 7i \\ 6.88e - 7i \\ -0.12i \\ 3.84 + 0.0045i \\ 8.60 + 4.81e - 7i \\ 12.89 + 0.03i \end{bmatrix}$$

$$V = \begin{bmatrix} 0.75 & 0 & -0.60 - 0.0019i & 0 & 0.07 + 0.00058i & 0 & 0.20 + 0.0011i & 0 & 0.17 + 0.0011i \\ 0 & -0.64 & 0 & 0.68 & 0 & 0 & 0 & -0.34 & 0 \\ -0.34 - 0.00024i & 0 & 0.08 + 0.0015i & 0 & 0.73 & 1.32e - 7i & -0.09 - 0.0018i & 0 & 0.57 - 0.00067i \\ 0 & 0 & 0 & 0 & 0 & 0 & -1.78e - 6 & 1 & 0 \\ 0 & 0 & 0 & 0 & 0 & 1 & 0 & 0 & -1.40e - 7i \\ -0.00068 & 0 & -0.03i & 0 & -0.03i & -1.59e - 7i & 1 & 3.56e - 6 & 0.00063 \\ 0.34 - 0.00024i & 0 & 0.08 - 0.0015i & 0 & 0.73 & -1.32e - 7i & 0.09 - 0.0018i & 0 & -0.57 - 0.00067i \\ 0 & 0.64 & 0 & 0.68 & 0 & 0 & 0 & 0.34 & 0 \\ 0.75 & 0 & 0.60 - 0.0019i & 0 & -0.07 + 0.00058i & 0 & 0.20 - 0.0011i & 0 & 0.17 - 0.0011i \end{bmatrix}$$

(b) $\alpha = 10^2$ (coupled case)

(i) Alfvén branch

$$A = \begin{bmatrix} -2.88 + 0.03i \\ 137.45i \\ 2.88 + 0.03i \end{bmatrix}$$

$$V = \begin{bmatrix} 0.54 - 5.69e - 03i & 0.54 + 0.02i & 0.64 \\ -0.71 & 0.71 & -0.02i \\ -0.54 - 5.69e - 03i & -0.54 + 0.02i & 0.64 \end{bmatrix}$$

(ii) Compressible branch

$$A = \begin{bmatrix} -10.95 + 0.09i \\ 104.34i \\ -2.77 + 0.04i \\ 0.43i \\ 137.45i \\ -0.08i \\ 2.77 + 0.04i \\ 135.71i \\ 10.95 + 0.09i \end{bmatrix}$$

$$V = \begin{bmatrix} 0.65 & 0.33 + 0.01i & -0.44 + 0.0051i & -0.44 - 0.02i & 0.03 - 0.0026i & 0.03 + 0.0026i & 0.17 - 0.0006i & 0.17 + 0.0099i & 0.15 - 0.0012i \\ 0.69 & -0.67 & 0.19i & -0.19i & -0.00031i & 0.00059i & 0.0078 & -0.0078 & 0.0061 \\ -0.23 - 0.01i & -0.11 + 0.02i & 0.04 + 0.0044i & 0.04 - 0.0091i & 0.53 - 0.0028i & 0.53 + 0.02i & -0.06 - 0.0078i & -0.06 + 0.01i & 0.60 \\ -0.57 & 0.57 & -0.02i & 0.05i & -0.02i & -0.02i & -0.22 & 0.54 & -0.0039 \\ 0.0054i & -0.0039i & -0.03 & 0.03 & -0.71 & 0.71 & 0.00081i & -0.00079i & -0.02i \\ -0.00047 & 0.000039 & -0.01i & -0.01i & -0.01i & -0.01i & 0.71 & 0.71 & 0.0004 \\ -0.23 + 0.01i & -0.11 - 0.02i & -0.04 + 0.0044i & -0.04 - 0.0091i & -0.53 - 0.0028i & -0.53 + 0.02i & -0.06 + 0.0078i & -0.06 - 0.01i & 0.60 \\ 0.15i & -0.11i & -0.69 & 0.70 & 0.02 & -0.02 & 0.02i & -0.02i & 0.02i \\ 0.65 & 0.33 - 0.01i & 0.44 + 0.0051i & 0.44 - 0.02i & -0.03 - 0.0026i & -0.03 + 0.0026i & 0.17 + 0.0006i & 0.17 - 0.0099i & 0.15 + 0.0012i \end{bmatrix}$$

Low beta regime ($B_0 = 10$)

$$A = \begin{bmatrix} -42.81 + 5.9i \\ 104.80i \\ -7.33 + 0.14i \\ 0.43i \\ 136.72i \\ -0.08i \\ 7.33 + 0.14i \\ 124.15i \\ 42.81 + 5.9i \end{bmatrix}$$

$$V = \begin{bmatrix} 0.14 + 0.0084i & 0.07 + 0.03i & -0.41 + 0.05i & -0.34 - 0.16i & 0.38 - 0.06i & 0.32 + 0.15i & 0.04 + 0.00037i & 0.03 + 0.02i & 0.62 \\ 0.66 & -0.65 & 0.23i & -0.27i & -0.05i & 0.09i & 0.0094 & -0.01 & 0.09 \\ 0.66 & 0.33 - 0.0080i & -0.30 + 0.0021i & -0.30 + 0.01i & -0.32 + 0.0019i & -0.32 - 0.03i & 0.18 + 0.0021i & 0.18 - 0.0050i & -0.10 - 0.0027i \\ -0.57 & 0.57 & -0.02i & 0.05i & -0.02i & -0.02i & -0.22 & 0.54 & -0.00040 \\ 0.10i & -0.07i & -0.46 & 0.46 & -0.53 & 0.53 & 0.01i & -0.01i & -0.02i \\ -0.00047 & 0.000039 & -0.01i & -0.01i & -0.01i & -0.01i & 0.71 & 0.71 & 0.000040 \\ 0.66 & 0.33 + 0.0080i & 0.30 + 0.0021i & 0.30 + 0.01i & 0.32 + 0.0019i & 0.32 - 0.03i & 0.18 - 0.0021i & 0.18 + 0.0050i & -0.10 + 0.0027i \\ 0.15i & -0.13i & -0.47 & 0.57 & 0.38 & -0.47 & 0.02i & -0.02i & 0.23i \\ 0.14 - 0.0084i & 0.07 - 0.03i & 0.41 + 0.05i & 0.34 - 0.16i & -0.38 - 0.06i & -0.32 + 0.15i & 0.04 - 0.00037i & 0.03 - 0.02i & 0.62 \end{bmatrix}$$

Acknowledgements. This work was supported by the International Space Science Institute (ISSI) in Bern, through ISSI International Team project 457: The Role of Partial Ionization in the Formation, Dynamics and Stability of Solar Prominences. We acknowledge valuable discussions with Prof. Andrew Hillier. This work was supported by the FWO grant 1232122N and a FWO grant G0B4521N. This project has received funding from the European Research Council (ERC) under the European Union’s Horizon 2020 research and innovation programme (grant agreement No. 833251 PROMINENT ERC-ADG 2018). This research is further supported by Internal funds KU Leuven, through the project C14/19/089 TRACESpace. The resources and services used in this work were provided by the VSC (Flemish Supercomputer Center), funded by the Research Foundation - Flanders (FWO) and the Flemish Government.

References

- Antiochos S., Klimchuk J.* A Model for the Formation of Solar Prominences // *ApJ*. IX 1991. 378. 372.
- Antolin Patrick.* Thermal instability and non-equilibrium in solar coronal loops: from coronal rain to long-period intensity pulsations // *Plasma Physics and Controlled Fusion*. I 2020. 62, 1. 014016.
- Brughmans N., Jenkins J. M., Keppens R.* The influence of flux rope heating models on solar prominence formation // *A&A*. XII 2022. 668. A47.
- Claes N., Keppens R.* Thermal stability of magnetohydrodynamic modes in homogeneous plasmas // *A&A*. IV 2019. 624. A96.
- Field G.* Thermal Instability. // *ApJ*. VIII 1965. 142. 531.
- Goedbloed H., Keppens R., Poedts S.* Waves and characteristics // *Magnetohydrodynamics of Laboratory and Astrophysical Plasmas*. 2019. 147–180.
- Gronke M., Oh S.* Cooling-driven coagulation // *MNRAS*. IX 2023. 524, 1. 498–511.
- Hermans, J., Keppens, R.* . Effect of optically thin cooling curves on condensation formation: Case study using thermal instability // *A&A*. 2021. 655. A36.
- Jenkins J., Keppens R.* Prominence formation by levitation-condensation at extreme resolutions // *A&A*. II 2021. 646. A134.
- Jerčić V., Keppens R.* Dynamic formation of multi-threaded prominences in arcade configurations // *A&A*. II 2023. 670. A64.
- Keppens R., Popescu Braileanu B., Zhou Y., Ruan W., Xia C., Guo Y., Claes N., Bacchini F.* MPI-AMRVAC 3.0: Updates to an open-source simulation framework // *A&A*. V 2023. 673. A66.
- Klimchuk J., Karpen J., Antiochos S.* Can Thermal Nonequilibrium Explain Coronal Loops? // *ApJ*. V 2010. 714, 2. 1239–1248.
- Li X., Keppens R., Zhou Y.* Coronal Rain in Randomly Heated Arcades // *ApJ*. II 2022. 926, 2. 216.
- Li X., Keppens R., Zhou Y.* Multithermal Jet Formation Triggered by Flux Emergence // *ApJ*. IV 2023. 947, 1. L17.
- Liakh V., Keppens R.* Rotational Flows in Solar Coronal Flux Rope Cavities // *ApJ*. VIII 2023. 953, 1. L13.
- Luna M., Karpen J., DeVore C.* Formation and Evolution of a Multi-threaded Solar Prominence // *ApJ*. II 2012. 746, 1. 30.
- Martínez-Gómez D., Oliver R., Khomenko E., Collados M.* Large Ion-neutral Drift Velocities and Plasma Heating in Partially Ionized Coronal Rain Blobs // *ApJ*. XII 2022. 940, 2. L47.
- Oliver R., Soler R., Terradas J., Zaqrashvili T. V.* Dynamics of Coronal Rain and Descending Plasma Blobs in Solar Prominences. II. Partially Ionized Case // *ApJ*. II 2016. 818, 2. 128.
- Parenti, S., Del Zanna, G., Vial, J.-C.* . Elemental composition in quiescent prominences // *A&A*. 2019. 625. A52.
- Parker E.* Instability of Thermal Fields. // *ApJ*. V 1953. 117. 431.
- Popescu Braileanu, B., Keppens, R.* . Two-fluid implementation in MPI-AMRVAC with applications to the solar chromosphere // *A&A*. 2022. 664. A55.
- Popescu Braileanu B., Lukin V. S., Khomenko E.* Magnetic field amplification and structure formation by the Rayleigh-Taylor instability // *A&A*. II 2023. 670. A31.
- Popescu Braileanu B., Lukin V. S., Khomenko E., de Vicente Á.* Two-fluid simulations of waves in the solar chromosphere. I. Numerical code verification // *A&A*. VII 2019. 627. A25.
- Popescu Braileanu B., Lukin V. S., Khomenko E., de Vicente Á.* Two-fluid simulations of Rayleigh-Taylor instability in a magnetized solar prominence thread. I. Effects of prominence magnetization and mass loading // *A&A*. II 2021a. 646. A93.
- Popescu Braileanu B., Lukin V. S., Khomenko E., de Vicente Á.* Two-fluid simulations of Rayleigh-Taylor instability in a magnetized solar prominence thread. II. Effects of collisionality // *A&A*. VI 2021b. 650. A181.
- Proga D., Waters T., Dyda S., Zhu Z.* Thermal Instability in Radiation Hydrodynamics: Instability Mechanisms, Position-dependent S-curves, and Attenuation Curves // *ApJ*. VIII 2022. 935, 2. L37.

- Schrijver C. J.* Catastrophic cooling and high-speed downflow in quiescent solar coronal loops observed with TRACE // *Sol. Phys.*. II 2001. 198, 2. 325–345.
- Smirnov B. M.* *Physics of Atoms and Ions.* 2003. XIII, 443.
- Snow, B. , Hillier, A. .* Collisional ionisation, recombination, and ionisation potential in two-fluid slow-mode shocks: Analytical and numerical results // *A&A.* 2021. 645. A81.
- Soler R., Carbonell M., Ballester J. L.* Magnetoacoustic waves in a partially ionized two-fluid plasma // *The Astrophysical Journal Supplement Series.* oct 2013b. 209, 1. 16.
- Soler R., Carbonell M., Ballester J. L., Terradas J.* Alfvén Waves in a Partially Ionized Two-fluid Plasma // *ApJ.* IV 2013a. 767, 2. 171.
- Terradas J., Luna M., Soler R., Oliver R., Carbonell M., Ballester J. L.* One-dimensional prominence threads. I. Equilibrium models // *A&A.* IX 2021. 653. A95.
- Voronov G. S.* A Practical Fit Formula for Ionization Rate Coefficients of Atoms and Ions by Electron Impact: $z=1-28$ // *Atomic Data and Nuclear Data Tables.* 1997. 65, 1. 1 – 35.
- Waters T., Proga D., Dannen R., Dyda S.* Dynamical Thermal Instability in Highly Supersonic Outflows // *ApJ.* VI 2022. 931, 2. 134.
- Xia C., Keppens R., Fang X.* Coronal rain in magnetic bipolar weak fields // *A&A.* VII 2017. 603. A42.
- Yadav, N. , Keppens, R. , Popescu Braileanu, B. .* 3D MHD wave propagation near a coronal null point: New wave mode decomposition approach // *A&A.* 2022. 660. A21.
- Zhou Y., Li X., Hong J., Keppens R.* Winking filaments due to cyclic evaporation-condensation // *A&A.* VII 2023. 675. A31.